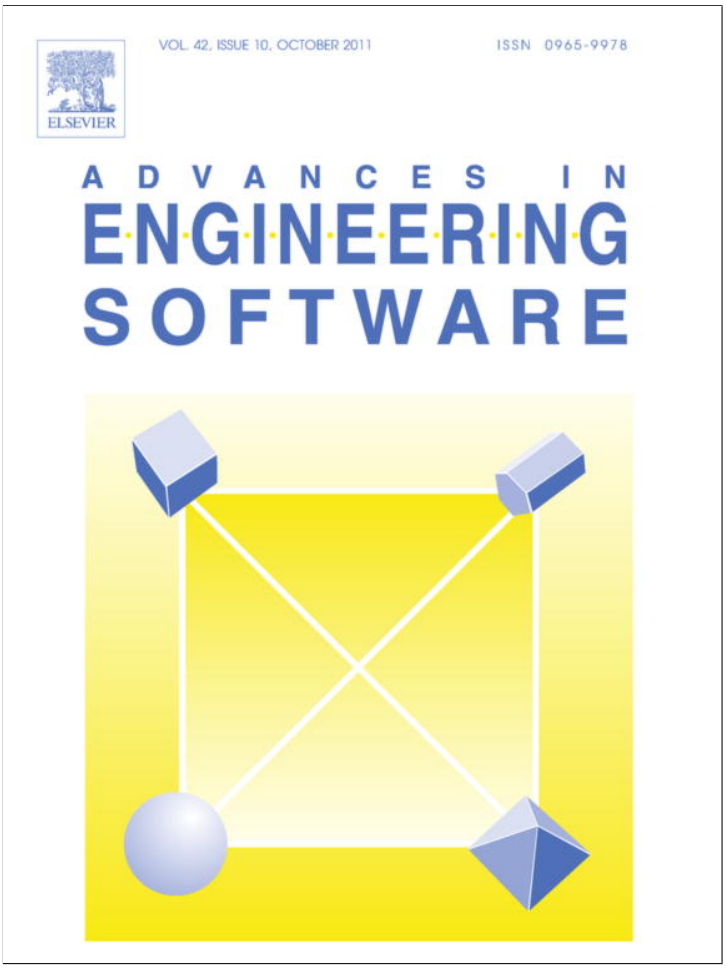

Advances in Engineering Software 42 (2011) 750–759

Contents lists available at ScienceDirect

Advances in Engineering Software

journal homepage: www.elsevier.com/locate/advengsoft

Simulation of ellipsoidal particle-reinforced materials with eigenstrain formulation of 3D BIE

Hang Ma [a,*], Jing-Bo Fang [b], Qing-Hua Qin [c]

[a] Department of Mechanics, College of Sciences, Shanghai University, Shanghai 200444, China
[b] Shanghai Institute of Applied Mathematics and Mechanics, Shanghai University, Shanghai 200072, China
[c] School of Engineering, Australian National University, Canberra, ACT 0200, Australia

ARTICLE INFO

Article history:
Received 22 September 2010
Received in revised form 9 May 2011
Accepted 10 May 2011

Keywords:
Eigenstrain
Eshelby tensor
Ellipsoidal particle
Boundary integral equation
Iterative method
Representative volume element

ABSTRACT

Based on the concepts of eigenstrain and equivalent inclusion of Eshelby for inhomogeneity problems, a computational model and its solution procedure are presented using the proposed three-dimensional (3D) eigenstrain formulation of boundary integral equations (BIE) for simulating ellipsoidal particle-reinforced (and/or void-weakened) inhomogeneous materials. In the model, the eigenstrains characterizing deformation behaviors of each particle embedded in the matrix are determined using an iterative scheme with the aid of the corresponding Eshelby tensors, which can be obtained beforehand either analytically or numerically. With the proposed numerical model, the unknowns of the problem appear only on the boundary of the solution domain, since the interface condition between particles/voids and the matrix is satisfied naturally. The solution scale of the inhomogeneity problem can thus be significantly reduced. Using the algorithm, the stress distribution and the overall elastic properties are identified for ellipsoidal particle-reinforced/void-weakened inhomogeneous materials over a representative volume element (RVE). The effects of a variety of factors on the overall properties of the materials as well as the convergence behavior of the algorithm are studied numerically, showing the validity and efficiency of the proposed algorithm.

1. Introduction

Determination of the elastic behavior of an inclusion embedded in a matrix is of considerable importance in a wide variety of physical and engineering problems. Following the pioneering work of Eshelby [1,2], inclusion and inhomogeneity problems have been a focus of solid mechanics for several decades. Due to Eshelby's work on an equivalent inclusion and eigenstrain solution, numerous investigations both analytical [3–9] and numerical [10–17] have been reported in the literature. In various physical problems, the eigenstrain can represent thermal mismatch, lattice mismatch, phase transformation, microstructural evolution, and intrinsic strains in residual stress problems [18]. Eshelby's solution is of great versatility and has been employed to address a wide range of physical problems in materials science, mechanics, and physics.

The analytical equivalent inclusion models available in the literature can be taken as the basis for predicting stress/strain distribution either within or outside the inhomogeneity and for further study of the mechanical performance of heterogeneous materials. However, the available solutions apply generally to only simple geometries such as single ellipsoidal, cylindrical and spherical inclusions in an infinite domain, because of the complexity of the mathematical expression and difficulty in solving the corresponding governing equations in 3D systems. Therefore, numerical methods including finite element methods (FEM), volume integral methods (VIM) and boundary element methods (BEM) have been used in the analysis of inhomogeneity problems involving various shapes and materials. The FEM may yield results for the entire composite materials, including results within the inhomogeneity [11], but the solution scale would be very large since both matrix and inhomogeneities must to be discretized. The VIM and the BEM seem more suitable than the FEM for the solution of inhomogeneity problems in comparison. In the VIM [12–14], the domains of inhomogeneity are represented by volume integrals, essentially simplifying the construction of the final matrix of the linear algebraic system to which the problem is reduced to some extent after the discretization. However, as the interfaces between matrix and inclusion need to be discretized in the VIM, it is suitable for small scale problems with only a few inhomogeneities. The situation in the application of the BEM to inclusion problems, often coupled with VIM [15,16], is much the same as that of the VIM in which problems of simple arrays of inclusions are solved on a small scale, for a similar reason to that in the VIM, i.e., unknowns appearing in

* Corresponding author.
E-mail address: hangma@staff.shu.edu.cn (H. Ma).

0965-9978/$ - see front matter © 2011 Elsevier Ltd. All rights reserved.
doi:10.1016/j.advengsoft.2011.05.013

the interfaces. For large-scale problems of inhomogeneity with the BEM [17], special techniques of fast multipole expansions [19] must be employed, which leads to complexity of the solution procedure.

To the authors' knowledge, the potential engineering applications of Eshelby's idea of equivalent inclusion and eigenstrain solution have not yet been fully explored in the area of computational treatment of materials with inhomogeneities [20]. With Eshelby's idea as the basis, Ma et al. [21] recently proposed the eigenstrain formulation of the BIE for modeling elliptical particle-reinforced materials in two-dimensional elasticity. In the present work, that computational model is extended to the three-dimensional case by incorporating the corresponding BEM for analyzing the stress/strain behavior of ellipsoidal particle-reinforced/void-weakened materials.

2. Eigenstrain formulations of BIE

In the present model, perfect adhesion between the particle and the matrix, both being isotropic materials, is assumed, so that the displacement continuity and the traction equilibrium still hold true along their interfaces. The solution domain considered is a finite region Ω filled with the matrix and inclusions, bounded by the outer boundary Γ. The domain of the inhomogeneity is denoted by Ω_I with the boundary Γ_I($\Gamma_I = \Omega_I \cap \Omega$). The displacement and stress fields of the problem can be described by the eigenstrain formulations of the BIE [21,22] as follows:

$$C(p)u_i(p) = \int_\Gamma \tau_j(q)u^*_{ij}(p,q)\,d\Gamma(q) - \int_\Gamma u_j(q)\tau^*_{ij}(p,q)\,d\Gamma(q) + \sum_{I=1}^{N_I}\int_{\Omega_I}\varepsilon^0_{jk}(q)\sigma^*_{ijk}(p,q)\,d\Omega(q) \tag{1}$$

$$C(p)\sigma_{ij}(p) = \int_\Gamma \tau_k(q)u^*_{ijk}(p,q)\,d\Gamma(q) - \int_\Gamma u_k(q)\tau^*_{ijk}(p,q)\,d\Gamma(q) + \sum_{I=1}^{N_I}\int_{\Omega_I}\varepsilon^0_{kl}(q)\sigma^*_{ijkl}(p,q)\,d\Omega(q) + \varepsilon^0_{kl}(p)O^*_{ijkl}(p,q) \tag{2}$$

where

$$O^*_{ijkl}(p,q) = \lim_{\Omega_\varepsilon\to 0}\int_{\Delta\Gamma_\varepsilon} x_l\tau^*_{ijk}(p,q)\,d\Gamma(q) \tag{3}$$

in which Ω_ε (surrounded by the boundary Γ_ε) represents an infinitesimal zone within Ω_I when the source point p approaches the field point q [23] and $x_l = x_l(q) - x_l(p)$. In Eqs. (1) and (2), u^*_{ij}, τ^*_{ij} and σ^*_{ij} stand for the Kelvin's fundamental solutions for displacements, tractions and stresses, respectively. u^*_{ijk}, τ^*_{ijk} and σ^*_{ijk} are correspondingly the derived fundamental solutions [21,22]. N_I is the total number of particles in the domain Ω.

In Eshelby and Mura's terminology [3], an inclusion is a bounded region within a material with the same material properties as the surrounding material but containing a stress-free transformation strain or eigenstrain. In contrast, an inhomogeneity (a particle) existing in a bounded region within a material has different material properties and may (or may not) contain an eigenstrain. Eshelby showed [1,2] that an inhomogeneity under loading can be simulated via an equivalent inclusion containing a fictitious eigenstrain, ε^0_{ij}, expressed by domain integrals in Eqs. (1) and (2), the so-called the eigenstrain formulations. The eigenstrains of particles here are determined using an iterative scheme, which will be described in detail in the following section. Obviously, the eigenstrains in each particle depend on the applied stresses or strains, the geometry of the particle, as well as the material constants of particle and matrix.

Eshelby's original work [1,2] related the constrained strain ε^C_{ij} developed in an inclusion located in an infinite matrix to the eigenstrain (the stress-free strain or the transformation strain) ε^0_{ij} via what is now widely known as the Eshelby tensor S_{ijkl}, that is

$$\varepsilon^C_{ij} = S_{ijkl}\varepsilon^0_{kl} \tag{4}$$

The Eshelby tensor S_{ijkl} is geometry dependent only, and generally takes the form of integrals. For simple geometries, the components of S_{ijkl} can be given explicitly and are available, for example, in the literature [1,4,9] or can be computed numerically [21] by

$$S_{ijkl} = \frac{1}{2}(\delta_{ik}\delta_{jl} + \delta_{il}\delta_{jk}) + C_{ijmn}\int_{\Gamma_I} x_l\tau^*_{mnk}(p,q)\,d\Gamma = \frac{1}{2}(\delta_{ik}\delta_{jl} + \delta_{il}\delta_{jk}) + \frac{1}{4\mu}\int_{\Gamma_I} x_l\left\{\tau^*_{ijk} + \tau^*_{jik} - \frac{2\nu}{1+\nu}\delta_{ij}\tau^*_{mmk}\right\}d\Gamma \tag{5}$$

where C_{ijkl} is the compliance tensor of the matrix, μ the shear modulus. By defining the Young's modulus ratio $\beta = E_I/E_M$, where the subscripts I and M represent the inhomogeneity (particle) and the matrix, respectively, the following relation holds true according to Hooke's law. If a particle is subjected to an applied strain ε_{ij}, it can be replaced by an equivalent inclusion without altering its stress state:

$$(1-\beta_1)\varepsilon^C_{ij} + \beta_2\delta_{ij}\varepsilon^C_{kk} - \varepsilon^0_{ij} - \frac{\nu_M}{1-2\nu_M}\delta_{ij}\varepsilon^0_{kk} = -(1-\beta_1)\varepsilon_{ij} - \beta_2\delta_{ij}\varepsilon_{kk} \tag{6}$$

where

$$\beta_1 = \frac{1+\nu_M}{1+\nu_I}\beta, \qquad \beta_2 = \frac{\nu_M}{1-\nu_M} - \frac{\nu_I}{1-2\nu_I}\beta \tag{7}$$

and ν is Poisson's ratio. Combining Eqs. (4) and (6), the eigenstrains in each particle can be estimated from the given applied strains.

3. Solution procedures

The present computational model for ellipsoidal particle-reinforced materials is solved numerically by way of the BEM [22]. In order to avoid domain discretization, the domain integrals in Eqs. (1) and (2) need to be transformed into boundary-type integrals before discretization, as [23]

$$\int_{\Omega_I}\sigma^*_{ijk}\,d\Omega = \int_{\Gamma_I} x_k\tau^*_{ij}\,d\Gamma \tag{8}$$

$$\int_{\Omega_I}\sigma^*_{ijkl}\,d\Omega + O^*_{ijkl} = \int_{\Gamma_I} x_l\tau^*_{ijk}\,d\Gamma \tag{9}$$

in which the eigenstrains in each particle are assumed to be constant. It is noted that the applied strains (or the applied stresses) over each particle are disturbed by other particles, especially those near the particle of interest, because the eigenstrain in a particle will induce a self-balanced stress field in both the particle and the matrix. In addition to the applied load, the eigenstrain-induced stresses outside the particle are superimposed on other particles. As a result, the applied strains with regard to the eigenstrains are corrected in an iterative way in the solution procedure. After discretization and incorporated with the boundary conditions, Eq. (1) can be written in matrix form as:

$$\mathbf{Ax} = \mathbf{b} + \mathbf{B}\boldsymbol{\varepsilon} \tag{10}$$

where $\mathbf{A}$ is the system matrix, $\mathbf{B}$ the coefficient matrix for eigenstrains, $\mathbf{b}$ the right vector related to the known quantities applied on the outer boundary, $\mathbf{x}$ the vector unknowns to be solved. $\boldsymbol{\varepsilon}$ is the eigenstrain vector of all the particles to be corrected in the iteration. It should be mentioned that the coefficients in $\mathbf{A}$, $\mathbf{B}$ and $\mathbf{b}$ are all constants, and thus need to be computed only once. At the starting point, the vector $\boldsymbol{\varepsilon}$ is assigned by initial values for the applied

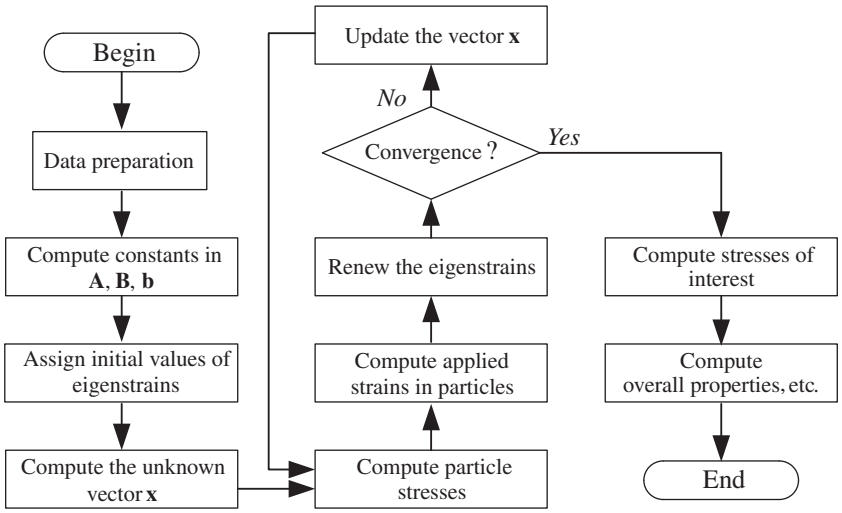

Fig. 1. Flowchart of the algorithm for the eigenstrain formulation of BIE.

strains via Eq. (2) at each position of the particles in the elastic state, computed irrespective of particles (i.e., the whole solution domain contains the homogeneous matrix only). Then the unknown vector **x** can be computed by the following iterative formulae:

$$\mathbf{x}^{(k+1)} = \mathbf{A}^{-1}\left(\mathbf{b} + \mathbf{B}\boldsymbol{\varepsilon}^{(k)}\right) \tag{11}$$

where k is the iteration count. Define the maximum iteration error as

$$\varepsilon_{\max} = \max\left|\left\{\boldsymbol{\varepsilon}^{(k)} - \boldsymbol{\varepsilon}^{(k-1)}\right\}\right| \tag{12}$$

which is the maximum difference of the eigenstrain components between two consecutive iterations. The convergent criterion in the present study is chosen as follows:

$$E_M\varepsilon_{\max} \leqslant 10^{-3} \tag{13}$$

where $E_M\varepsilon_{\max}$ corresponds to the maximum difference of the 'stress' components among total equivalent inclusions between two consecutive iterations and E_M is the Young's modulus of the matrix material. If the criterion (13) is not met, then the stress states at each particle, Ω_I, are computed using a modified Eq. (2), as follows, with the renewed vector **x** and then the applied strains to update the values of the eigenstrains:

$$\begin{aligned}\sigma_{ij}(p) = &\int_\Gamma \tau_k(q)u^*_{ijk}(p,q)\,d\Gamma(q) - \int_\Gamma u_k(q)\tau^*_{ijk}(p,q)\,d\Gamma(q)\\ &+ \sum_{J=1,J\neq I}^{N_I} \varepsilon^0_{kl}(q)\int_{\Gamma_J} x_l\tau^*_{ijk}(p,q)\,d\Gamma(q),\\ &p\in\Omega_I,\quad I=1,\ldots,N_I\end{aligned} \tag{14}$$

It should be noted here that in Eq. (14), the current particle has been excluded because the stress state at the due place is generated, in addition to the applied load, by the disturbances of all other particles in the solution domain. The principal steps in the solution procedures can be summarized as follows:

(a) Compute the constant coefficients in **A**, **B** and **b** in Eq. (1).
(b) Assign the vector **ε** an initial value which is the solution to the applied strains via Eq. (2) at the corresponding position of each particle without the presence of particles (i.e., the whole solution domain contains the homogeneous matrix only).
(c) Compute the unknown vector **x** using the iterative formulae (11) with the current eigenstrain vector **ε**.
(d) Check the convergent criterion (12).
(e) If the criterion (13) is not met, perform the following:
  (i) Compute the current stresses in each particle using Eq. (14) with the current particle absent at the corresponding place.
  (ii) Compute the current applied strains in each particle using Hooke's Law.
  (iii) Renew the eigenstrain vector **ε** using Eq. (6).
  and then return to the step (c). Otherwise proceed to the next step (f).
(f) Compute the stresses of interest or the overall properties, etc.

It can be seen that the determination of eigenstrains in each particle is the crucial step where the Eshelby tensor plays an essential role. Although some explicit expressions exist in the literature

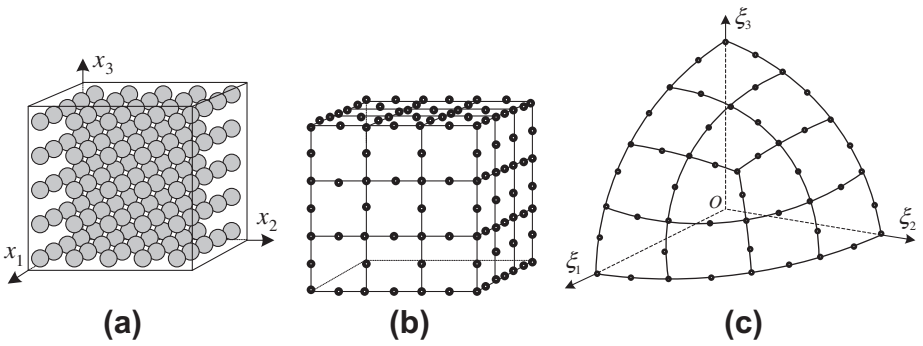

Fig. 2. (a) RVE with triply periodically spaced particles; (b) element mesh of the outer surface; and (c) element mesh for the boundary of a particle in one octant.

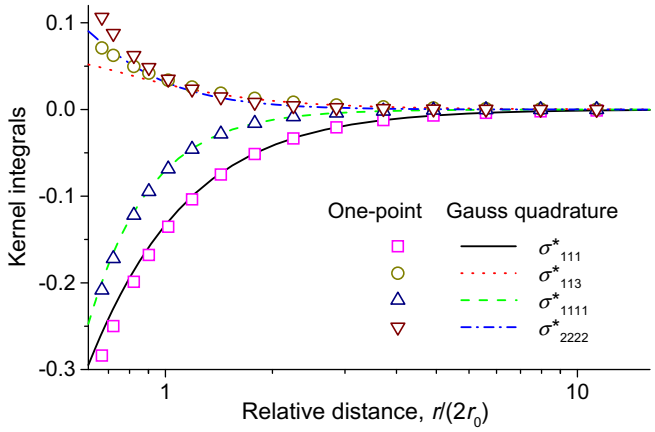

Fig. 3. Comparison of values of kernel integrals between one-point computing and Gauss quadrature.

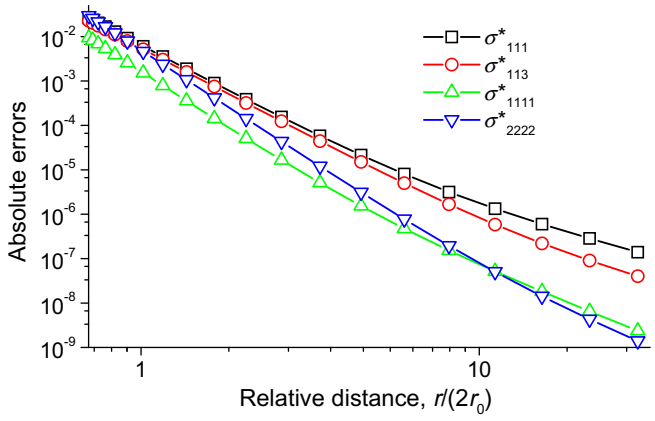

Fig. 4. Comparison of absolute errors between one-point computing and Gauss quadrature.

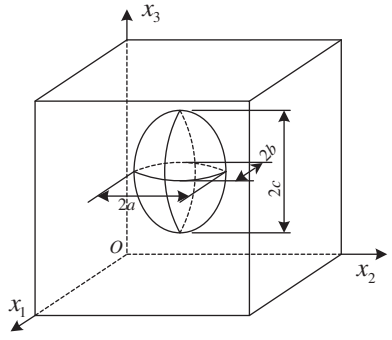

Fig. 5. A single ellipsoidal particle in a RVE.

for simple cases, in general the Eshelby tensor can always be obtained conveniently via the numerical means. The flow chart of the algorithm is shown in Fig. 1.

4. Numerical examples

In this section, the technique of one-point computing [24] is first assessed and used for evaluating domain integrals in Eqs. (1) and (2), in order to improve the efficiency of the proposed algorithm further. As mentioned at the beginning of Section 2, perfect adhesion between particle and matrix is assumed in the present computational model, which is solved by way of the BEM, so that the displacement continuity and the traction equilibrium hold true

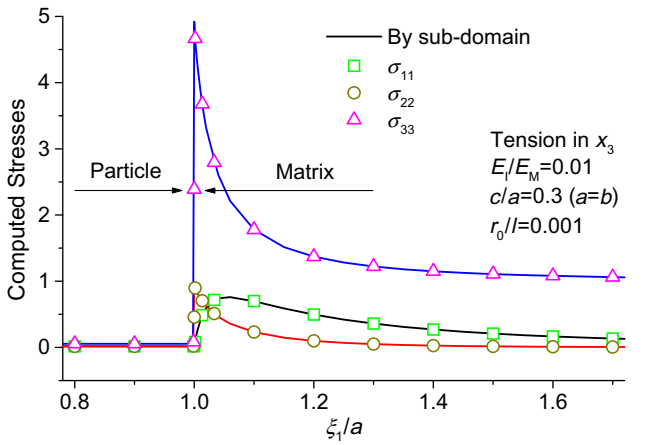

Fig. 6. Comparison of the computed stresses across the interface of a single soft particle in tension with those using BEM with the sub-domain technique.

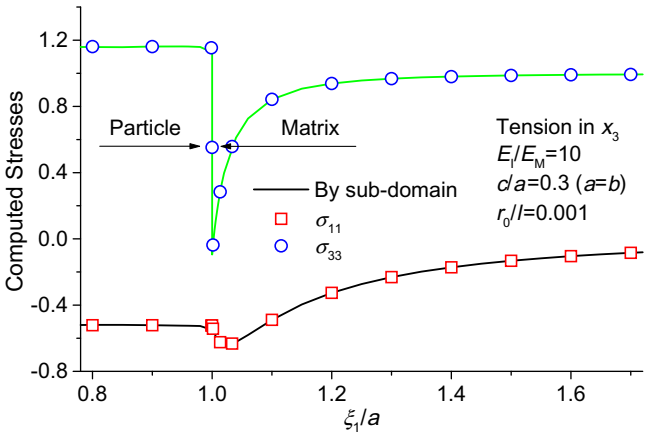

Fig. 7. Comparison of the computed stresses across the interface of a single hard particle in tension with those using BEM with the sub-domain technique.

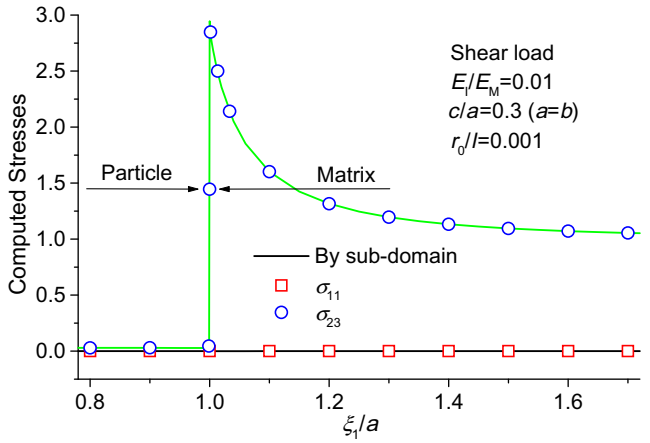

Fig. 8. Comparison of the computed stresses across the interface of a single soft particle in pure shear with those using BEM with the sub-domain technique.

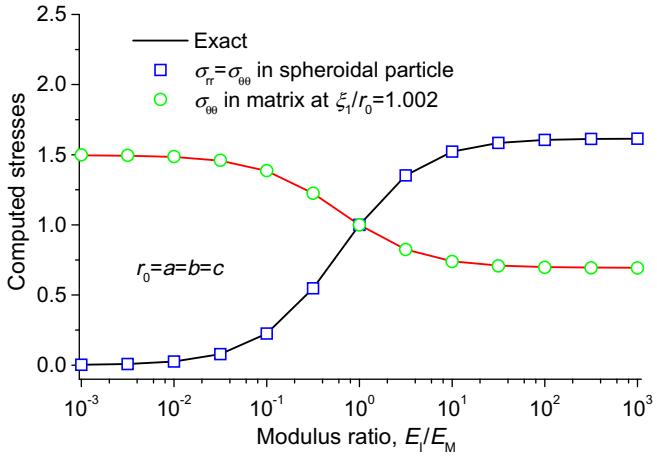

Fig. 9. Comparison of the computed stresses as a function of modulus ratio, E_I/E_M, for a spheroidal particle in triaxial tension.

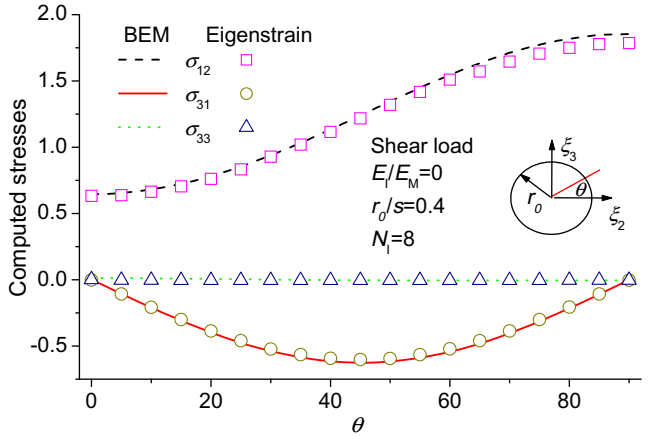

Fig. 12. Comparison of the computed stresses along a quarter arc outside a hole in pure shear.

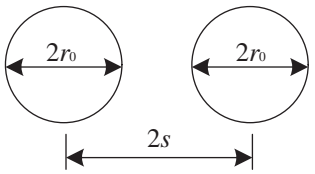

Fig. 10. The particle spacing 2s and the equivalent radius r_0.

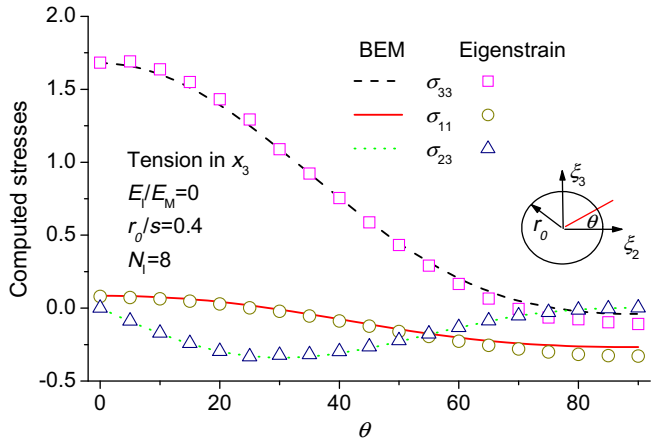

Fig. 11. Comparison of the computed stresses along a quarter arc outside a hole in single tension.

along their interfaces. To demonstrate the accuracy and efficiency of the proposed algorithm, the results of stresses across the interfaces for a simple example are obtained using the present algorithm and compared with those from the conventional BEM. Further, the overall properties and the stress distributions of a representative volume element (RVE) in a particle-reinforced material are identified using the proposed model. The convergent performance of the algorithm is assessed through investigating the effect of various factors on the number of iterations.

In the following analysis, a cube as shown in Fig. 2a is chosen as the RVE containing triply periodically spaced ellipsoidal particles. The element mesh used is shown in Fig. 2b for the outer boundary of the RVE and in Fig. 2c for the interface between matrix and particle (an octant of particle surface). It should be pointed out that the domain cells are no longer required as the domain integrals have been transformed into the boundary-type. It should also be mentioned that the interface discretization makes no contribution to the degrees of freedom of the problem for the present algorithm. The purpose of the discretization is only for numerical evaluation of the boundary-type integrals in Eqs. (8) and (9), when the distances between p and q are relatively small. In all the examples, the Poisson's ratios are taken to be $v_I = v_M = 0.3$.

4.1. One-point computing

Instead of using Eqs. (8) and (9) by Gauss quadrature to evaluate the domain integrals in Eqs. (1) and (2) and considering the properties of kernel functions explained in [24], the efficiency of the algorithm can be further improved by introducing the technique of one-point computing under certain appropriate conditions as follows:

$$\int_{\Omega_I} \sigma^*_{ijk}\, d\Omega \approx V_I \sigma^*_{ijk} \tag{15}$$

$$\int_{\Omega_I} \sigma^*_{ijkl}\, d\Omega \approx V_I \sigma^*_{ijkl} \tag{16}$$

where V_I stands for the volume of Ω_I and $O^*_{ijkl} = 0$ in Eq. (9) for $p \in \Omega \setminus (\Omega_I \cup \Gamma_I)$ (the source point p is outside the Ω_I). The integral values and the absolute errors as a function of relative distance, $r/(2r_0)$, are compared in Figs. 3 and 4, respectively, using the two computing methods, one-point computing and Gauss quadrature, over a spheroidal domain with a radius r_0, where r represents the distance from p to the center of the spheroidal domain. It is evident from both Figs. 3 and 4 that the one-point computing can achieve acceptable accuracy if the distances, $r/(2r_0)$, are relatively large, which is the most cases when p is outside the current Ω_I since the difference in the integral values between the two methods becomes negligibly small with the increase of the relative distance, $r/(2r_0)$. In the present work, $r/(2r_0) = 5$ serves as the criterion to switch the methods between one-point computing and Gauss quadrature around closed interfaces.

4.2. Stress distributions in a cube with a single particle

In order to assess the model with the eigenstrain formulation, the stresses across the interface of a single particle in the RVE as shown in Fig. 5 are computed using the present algorithm and compared with the exact solutions for a spheroidal particle and with the numerical solutions for ellipsoidal particles using

Table 1
Comparison of the degrees of freedom and CPU times for the two algorithms.

N_I	Degree of freedom		CPU time (s)	
	BEM	Eigenstrain	BEM	Eigenstrain
1	1362	492	154	12.7
2	2232	492	283	14.8
4	3972	492	1223	16.6
8	7452	492	11,348	20.4

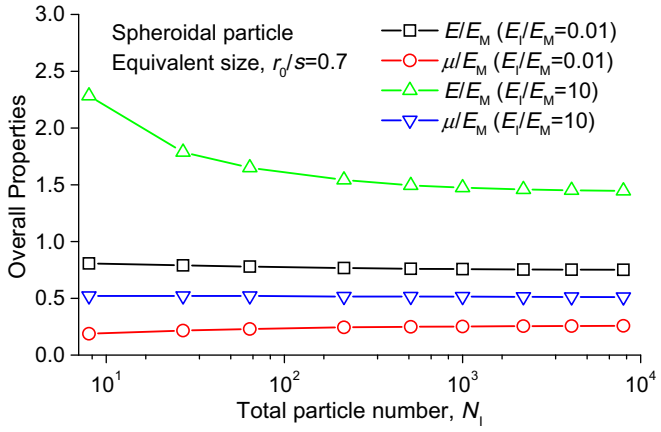

Fig. 13. Overall properties of the RVE with spheroidal particles as a function of total particle number, N_I, where the equivalent sizes, r_0/s, are kept constant.

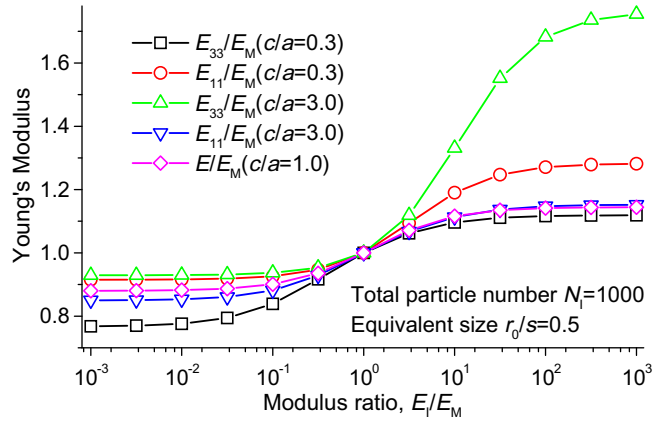

Fig. 14. Young's modulus of the RVE as a function of modulus ratio, E_I/E_M.

conventional BEM with sub-domain techniques. As shown in Fig. 5, a, b and c are three half radii of the ellipsoidal particle, which is placed at the center of the cube. In the present work, the shape of the ellipsoidal particle is chosen as oblate ($a = b > c$) or prolate ($a = b < c$). However, for the spheroidal particle, $a = b = c = r_0$. Define the equivalent radius r_0 for ellipsoidal particles as

$$r_0 = \sqrt[3]{abc} \tag{17}$$

for the purpose of comparing the relative sizes of different particles with the RVE. $r_0/l = 0.001$ is used in the computation, where l stands for the side length of the cube RVE. The stresses are computed across the interface of the particle along the ξ_1 axis as shown Fig. 2c, where $\xi_1 \| x_1$ in Fig. 5. On the interface, $\xi_1/a = 1$. To show the stress behavior when the computing point is very close to the interface, the technique of distance transformation [25] is utilized

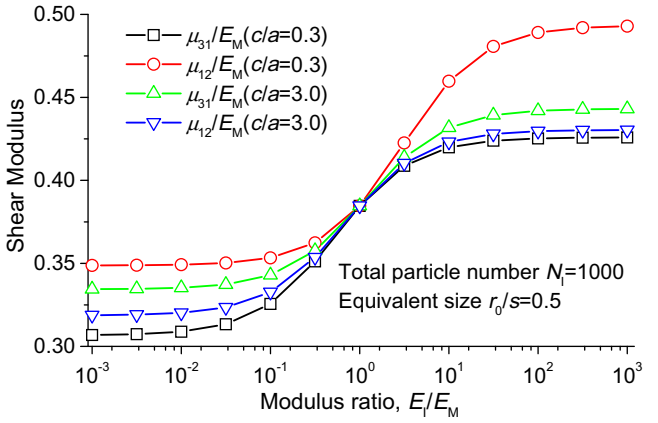

Fig. 15. Shear modulus of the RVE as a function of modulus ratio, E_I/E_M.

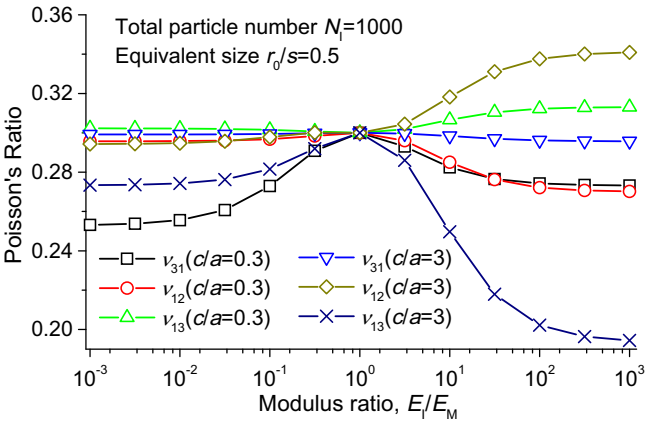

Fig. 16. Poisson's ratio of the RVE as a function of modulus ratio, E_I/E_M.

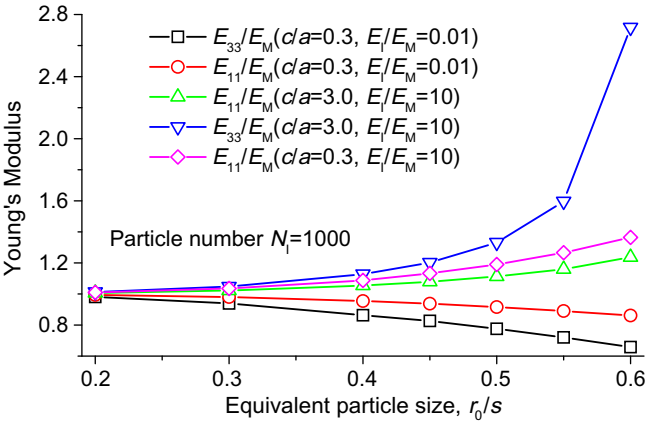

Fig. 17. Young's modulus of the RVE as a function of equivalent particle size, r_0/s.

to handle the nearly singularity of integral kernels. The stresses very close to the interface are evaluated at the locations $\xi_1/a = 0.998$ and $\xi_1/a = 1.002$, respectively.

The effect of particle stiffness on stress distribution is studied by computing the stresses across the interface of a soft and a hard particle in single tension in x_3 direction with unit traction load $\sigma_{33} = 1$, compared in Figs. 6 and 7, respectively, and the stresses of a soft particle in pure shear with unit shear load $\sigma_{23} = \sigma_{32} = 1$ are presented in Fig. 8 for the sake of comparison. It can be seen

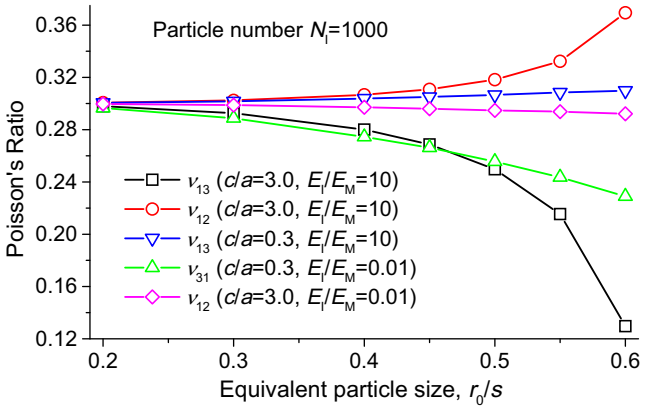

Fig. 18. Poisson's ratio of the RVE as a function of equivalent particle size, r_0/s.

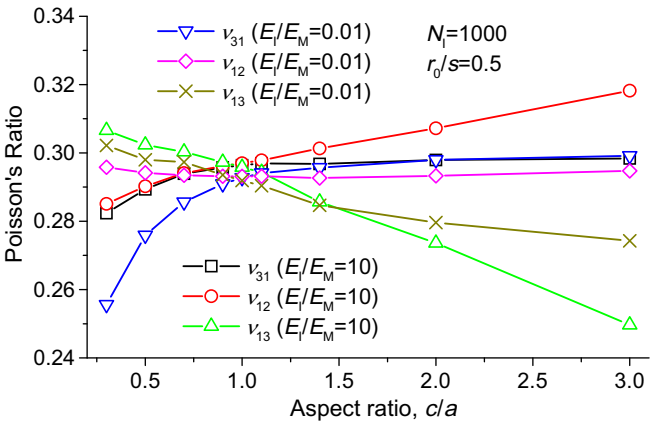

Fig. 21. Poisson's ratio of the RVE as a function of aspect ratio, c/a.

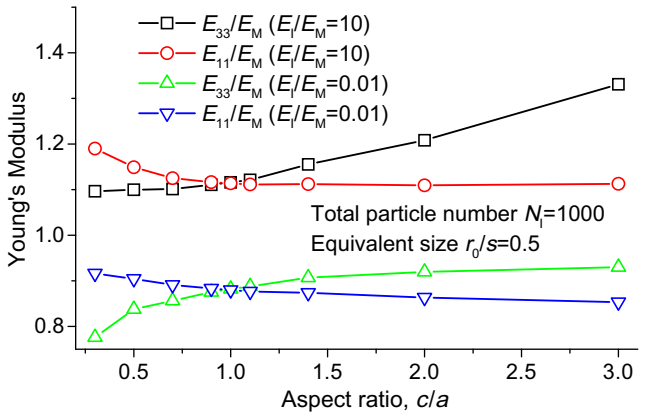

Fig. 19. Young's modulus of the RVE as a function of aspect ratio, c/a.

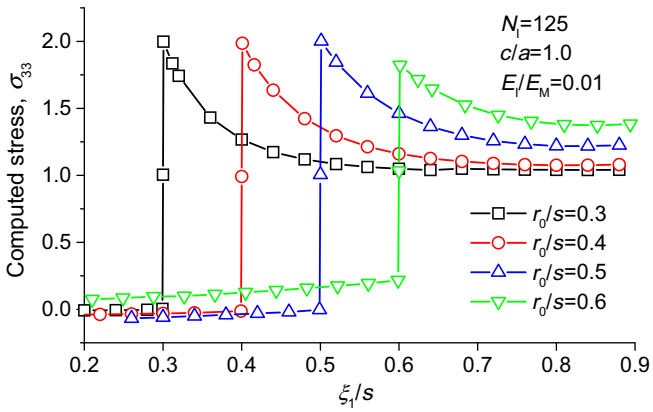

Fig. 22. Stress distributions across the interface of a soft spheroidal particle placed at the center of the RVE with various values of r_0/s.

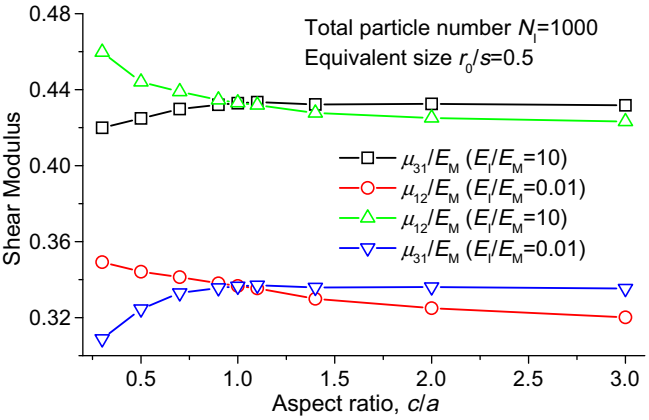

Fig. 20. Shear modulus of the RVE as a function of aspect ratio, c/a.

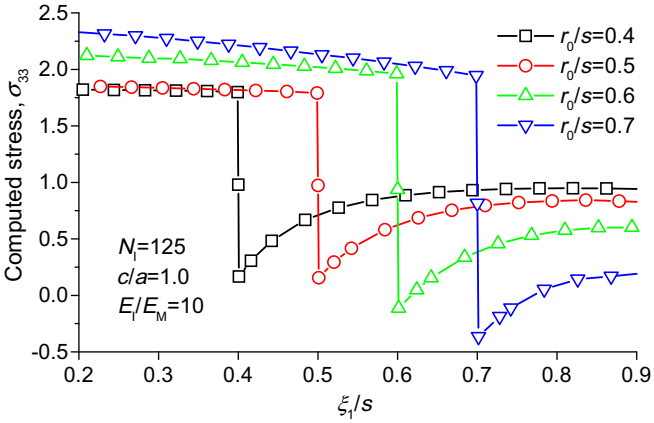

Fig. 23. Stress distributions across the interface of a hard spheroidal particle placed at the center of the RVE with various values of r_0/s.

from the three figures that the stresses are constant inside the particle as expected. It is found that the computed tangential stresses in tension and the shear stress in shear load all have a jump across the interface using the traditional BEM with the sub-domain technique computed on the interface, or more definitely, at the two corresponding places in boundaries of the two sub-domains. However, these computed stress components using the eigenstrain formulation show almost exactly the same behavior. It is interesting to see from Figs. 6–8 that the stress components which have jumps on the interface computed using the eigenstrain formulation take just the average values of the two sides, the particle and the matrix.

Nevertheless, it is observed that the stress components which have jumps computed with the present algorithm at the places in the matrix very close to the interface have tiny differences from those just on the interface computed with the sub-domain method.

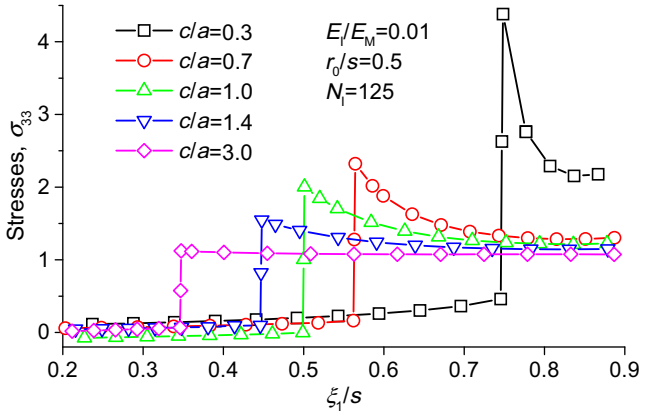

Fig. 24. Stress distributions across the interface of a soft ellipsoidal particle placed at the center of the RVE with various aspect ratios c/a.

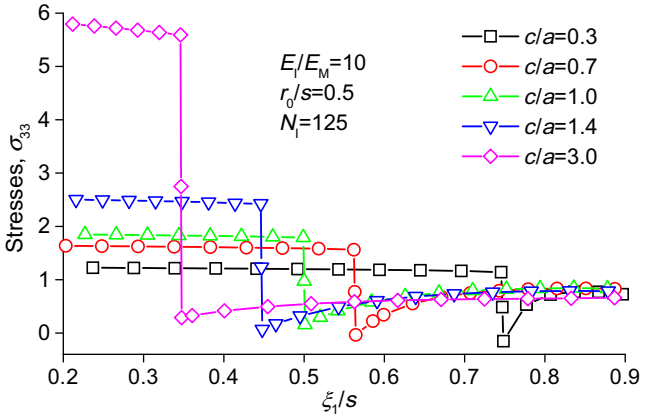

Fig. 25. Stress distributions across the interface of a hard ellipsoidal particle placed at the center of the RVE with various aspect ratios, c/a.

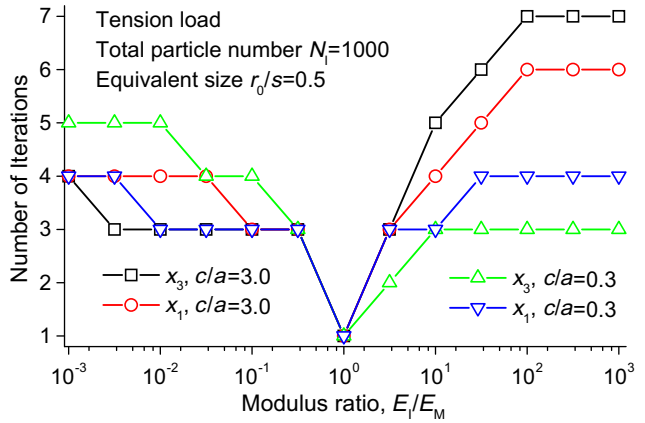

Fig. 26. Required number of iterations of the algorithm in tension with respect to the modulus ratio, E_I/E_M.

Fig. 9 gives the comparison of stresses in both the spheroidal particle and the matrix as a function of the modulus ratio, E_I/E_M, in triaxial tension load $\sigma_{11} = \sigma_{22} = \sigma_{33} = 1$ with the exact solutions [14]. The stresses in the matrix are computed at the place $\xi_1/r_0 = 1.002$, very close to the interface. The computed results show the validity and accuracy of the present algorithm.

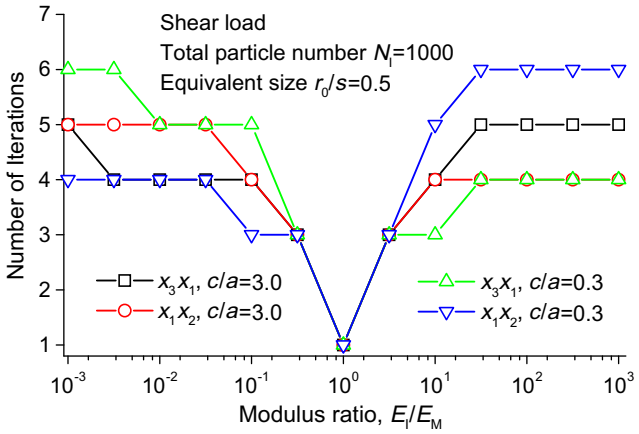

Fig. 27. Required number of iterations of the algorithm in shear with respect to the modulus ratio, E_I/E_M.

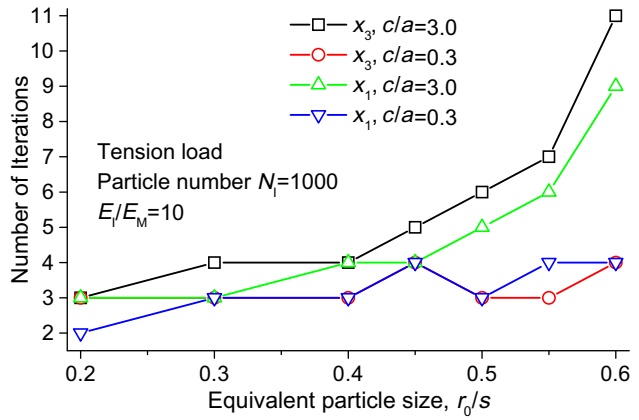

Fig. 28. Required number of iterations of the algorithm in tension with respect to the equivalent particle size, r_0/s, with hard particles.

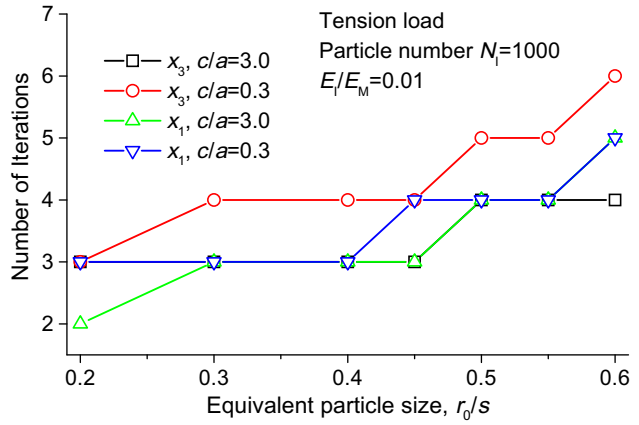

Fig. 29. Required number of iterations of the algorithm in tension with respect to the equivalent particle size, r_0/s, with soft particles.

4.3. Stress distributions in a cube with multiple empty holes

In order to check the model further with the eigenstrain formulation, the stress distributions in the matrix of the RVE with $N_I = 8$ spheroidal empty holes are computed using the present algorithm

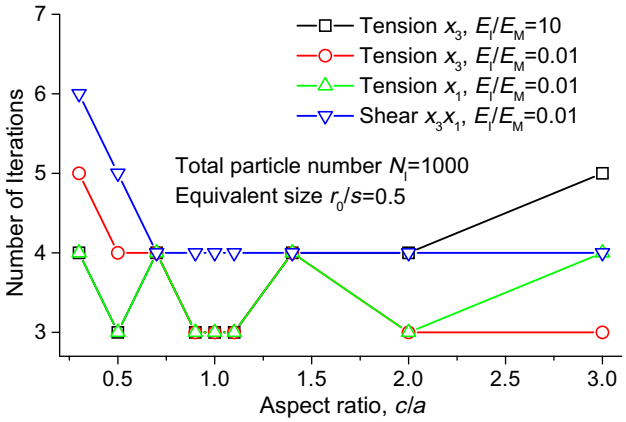

Fig. 30. Required number of iterations of the algorithm with respect to the aspect ratio, c/a.

and compared with the numerical solutions using the conventional BEM. In the computation, the RVE used is loaded with unit load in either single tension or pure shear. The equivalent particle or hole size, r_0/s, is defined dimensionlessly by the ratio of the equivalent radius and the half spacing between particles, as shown in Fig. 10. The equivalent size is set as $r_0/s = 0.4$ in this example for the RVE with 8 holes.

The stresses are computed along a quarter arc with the radius $r = 1.1r_0$ outside a hole in the matrix of the RVE while the local coordinate ξ_1 (Fig. 1a and c, $\xi_k//x_k$, k = 1,2,3) is kept constant, as shown in Figs. 11 and 12, respectively, under single tension and pure shear. It is shown from Figs. 11 and 12 that the computed results with the proposed algorithm using the eigenstrain formulation are in well agreement with those of the conventional BEM. As the degree of freedom increases very fast with the number of particles, the computing program using the BEM does not work on the present desktop computer (Intel Pentium Dual CPU, 1.60GNz), the comparison between the two algorithms cannot be performed for the RVE containing more particles. However, there is no such limitation for the proposed algorithm using the eigenstrain formulation.

The degree of freedom and CPU time of the two algorithms, the eigenstrain formulation and the BEM, are listed in Table 1 by running the two programs on the desktop computer under the tension load, showing the sharp differences in efficiency. For the BEM, the most part of the CPU time is spent for solving the system matrix, the degree of which increases very fast with the number of particles. The increase of the CPU time follows a geometrical series. In comparison, the number of degree of freedom for the eigenstrain formulation remains constant. The finite CPU time increased is spent only in the iteration, showing the high efficiency of the proposed algorithm, especially for the 3D problem.

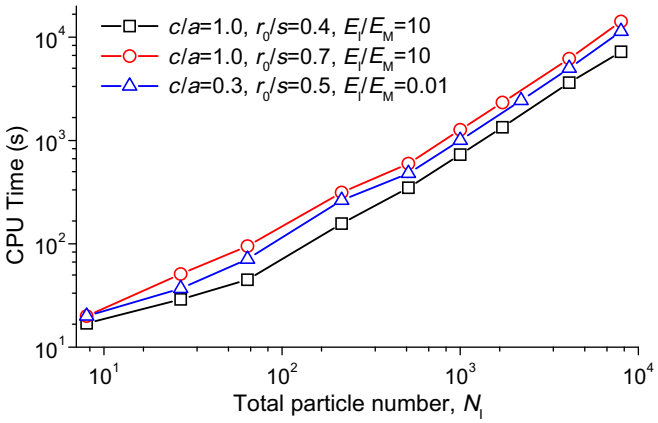

Fig. 31. CPU time of the algorithm as a function of total particle number, N_I.

4.4. Overall properties

In the computation, the RVE used is loaded with unit load in either single tension or pure shear. The results for the overall properties of the RVE with triply periodically spaced spheroidal particles as a function of the total particle number, N_I, are shown in Fig. 13, where the equivalent sizes, r_0/s, are kept constant, which means that the volume fraction of particles in the RVE remains constant. In this case, the overall properties are isotropic. It can be seen that the values of the computed overall properties become stable when $N_I \geqslant 1000$, showing that the boundary effect can be neglected, so that $N_I = 1000$ is chosen in the following examples.

The Young's modulus, shear modulus and Poisson's ratio of the RVE as a function of the modulus ratio, E_I/E_M, are presented in Figs. 14–16 with $N_I = 1000$, where c/a is the aspect ratio of particles. If $c/a = 1$ the particles are spheroidal and the overall properties become isotropic. It should be pointed out that $E_I/E_M = 10^{-3}$ behaves almost like holes whereas $E_I/E_M = 10^3$ corresponds to rigid particles in the matrix. It can be seen from Figs. 14 and 15 that for either Young's or shear moduli, the most effective range of the modulus ratio to the overall properties is between $E_I/E_M = 0.1$ and $E_I/E_M = 10$, while the stagnancy of the properties can be observed when E_I/E_M is very small or very large, similar to observations in the two-dimensional case [21]. However, the Poisson's ratio behaves in a very complex relationship with the modulus ratio, E_I/E_M, as shown in Fig. 16.

The study of the effect of equivalent particle size on the overall properties of the RVE, the Young's moduli and the Poisson's ratios of the RVE are presented in Figs. 17 and 18, respectively, as a function of equivalent particle size r_0/s. The two figures show monotonic variations as expected since the equivalent particle size corresponds directly to the volume fraction of particles in the RVE. With the increase of r_0/s, the Young's modulus of the RVE decreases with soft particles but increases with hard particles. However, the Poisson's ratio of the RVE shows diverse behaviors with r_0/s, as shown in Fig. 18.

Figs. 19–21 show the effects of aspect ratio, c/a, on Young's modulus, the shear modulus and Poisson's ratio of the RVE when the equivalent particle size, r_0/s, is kept constant. It is seen from Figs. 19 and 20 that the value of E_{33} increases monotonically with an increase in the value of the aspect ratio for the RVE with both hard and soft particles. It is interpreted that with the increase of the aspect ratio, c/a, the strengthening effect increases for hard particles but the weakening effect decreases for soft particles. In contrary, the value of E_{11} shows exactly the opposite behavior. The values of the shear moduli, μ_{31} and μ_{12}, behave very similarly to those of E_{33} and E_{11}, respectively, owing to the similar effects. It is evident from Fig. 21, however, that the values of the Poisson's ratio again behave in a more complex fashion with the increase of the aspect ratio, c/a.

4.5. Stress distributions of a cube with multiple particles

The stress distribution for a RVE with a single particle was studied in Section 4.2. This section presents an investigation of the stress distributions of a cube with multiple particles. The stress distribution across the interface of the particle at the center of the RVE with a total particle number $N_I = 125$ (Fig. 2a) under single tension of unit load $\sigma_{33} = 1$ is presented in Figs. 22 and 23, respectively, for soft and hard spheroidal particles with various

equivalent particle sizes, r_0/s. The stresses are computed across the interfaces of the particle along the ξ_1 axis as shown in Fig. 2c where $\xi_1 \| x_1$ in Fig. 5. On various interfaces there are $\xi_1/s = r_0/s$. The stresses very close to the interfaces are evaluated at $\xi_1/s = (1 \pm 0.002) \times r_0/s$ and all stresses take peak values at the sides of matrix. It can be seen from Figs. 22 and 23 that the distributions inside the particles are consistent with the inference of constant stresses or strains inside a particle with a simple shape by Eshelby [1,2] when the equivalent particle sizes are relatively small. However, the agreement becomes less consistent with that inference when the equivalent particle sizes are relatively large, for examples, $r_0/s = 0.6$ for soft particle in Fig. 22 and $r_0/s = 0.7$ for hard particle in Fig. 23, reflecting the stronger interference among particles.

The stress distributions for soft and hard ellipsoidal particles are presented in Figs. 24 and 25, respectively, as a function of ξ_1/s with various aspect ratios, c/a, while the equivalent particle sizes, r_0/s, is kept constant. The results of the computed stress distributions show further the validity and the effectiveness of the present algorithm.

4.6. Convergence behavior

The convergence behavior of the proposed algorithm is investigated by examining the required number of iterations. Figs. 26–30 show that the number of iterations varies with a variety of factors including the modulus ratio, the loading mode, the equivalent particle size or volume fraction and the shape of particles, which is considered to reflect the effects on or the disturbances to the stress states at the locations among particles. The required number of iterations of the algorithm with respect to the modulus ratio, E_I/E_M, is presented in Figs. 26 and 27, respectively, for the RVE being in tension and pure shear. It is considered that the value of the modulus ratio reflects the degree of mismatch between the materials of particles and matrix.

To study the effect of particle stiffness on the convergence behavior, Figs. 28 and 29 present the required number of iterations of the algorithm as a function of the equivalent particle size, r_0/s, for the RVE with hard and soft particles, respectively. It can be seen that the number of iterations increases monotonically with the increase of equivalent particle size, reflecting an increased disturbance of the particles. The required number of iterations of the algorithm with respect to the aspect ratio, c/a, is presented in Fig. 30, showing the effect of particle shape on the disturbances among particles while those of spheroidal particles are in general the smallest. Fig. 31 shows the CPU time of the algorithm as a function of total particle number, N_I. It is approximately a linear function of N_I. In summary, two principal factors need to be considered that influence the convergence behavior of the present algorithm. The first factor is the mutual disturbances of the stress states among the particles, and the second factor is the mismatches between the particles and the matrix.

5. Conclusions

An efficient computational model and solution procedure are presented for simulating ellipsoidal particle-reinforced composites using the proposed three-dimensional eigenstrain formulation of the BIE in the present study. As the unknowns appear only on the boundary of the solution domain, the solution scale of the problem with the present model remains fairly small in comparison with the conventional algorithm using the FEM or the BEM. To further improve the efficiency of the algorithm, one point computing is examined and employed in the algorithm. The results for the overall properties and stress distributions are presented for a RVE with single or multiple particles. The effects of various factors, including the overall properties of particle-reinforced composites, are examined. It is found that the tangential stresses on the interface from the eigenstrain formulation simply take the average values of the two sides, the particle and the matrix. The effectiveness and efficiency of the proposed algorithm as well as the convergent performance of the solution procedure are assessed numerically.

Acknowledgement

The work was supported by the National Natural Science Foundation of China (Grant No. 10972131).

References

[1] Eshelby JD. The determination of the elastic field of an ellipsoidal inclusion and related problems. Proc Roy Soc London 1957;A241:376–96.
[2] Eshelby JD. The elastic field outside an ellipsoidal inclusion. Proc Roy Soc London 1959;A252:561–9.
[3] Mura T, Shodja HM, Hirose Y. Inclusion problems (part 2). Appl Mech Rev 1996;49:S118–27.
[4] Federico S, Grilloc A, Herzog W. A transversely isotropic composite with a statistical distribution of spheroidal inclusions: a geometrical approach to overall properties. J Mech Phys Solids 2004;52:2309–27.
[5] Cohen I. Simple algebraic approximations for the effective elastic moduli of cubic arrays of spheres. J Mech Phys Solids 2004;52:2309–27.
[6] Franciosi P, Lormand G. Using the radon transform to solve inclusion problems in elasticity. Int J Solids Struct 2004;41:585–606.
[7] Shen LX, Yi S. An effective inclusion modal for effective moluli of heterogeneous materials with ellipsoidal inhomogeneities. Int J Solids Struct 2001;38:5789–805.
[8] Zhang X, Sharma P. Inclusions and inhomogeneities in strain gradient elasticity with couple stresses and related problems. Int J Solids Struct 2005;42:2851–3833.
[9] Feng XQ, Mai YW, Qin QH. A micromechanical model for interpenetrating multiphase composites. Comput Mater Sci 2003;28:486–93.
[10] Doghri I, Tinel L. Micromechanics of inelastic composites with misaligned inclusions: numerical treatment of orientation. Comput Methods Appl Mech Eng 2006;195:1387–406.
[11] Kakavas PA, Kontoni DN. Numerical investigation of the stress field of particulate reinforced polymeric composites subjected to tension. Int J Numer Methods Eng 2006;65:1145–64.
[12] Kanaun SK, Kochekseraii SB. A numerical method for the solution of thermo- and electro-static problems for a medium with isolated inclusions. J Comput Phys 2003;192:471–93.
[13] Lee J, Choi S, Mal A. Stress analysis of an unbounded elastic solid with orthotropic inclusions and voids using a new integral equation technique. Int J Solids Struct 2001;38:2789–802.
[14] Dong CY, Lo SH, Cheung YK. Numerical solution of 3D elastostatic inclusion problems using the volume integral equation method. Comput Methods Appl Mech Eng 2003;192:95–106.
[15] Qin QH, Yang QS. Macro-micro theory on multifield behaviour of heterogeneous materials. Beijing: Higher Education Press & Springer; 2008.
[16] Dong CY, Lee KY. Effective elastic properties of doubly periodic array of inclusions of various shapes by the boundary element method. Int J Solids Struct 2006;43:7919–38.
[17] Liu YJ, Nishimura N, Tanahashi T, Chen XL, Munakata H. A fast boundary element method for the analysis of fiber-reinforced composites based on a rigid-inclusion model. ASME J Appl Mech 2005;72:115–28.
[18] Ma H, Deng HL. Nondestructive determination of welding residual stresses by boundary element method. Adv Eng Softw 1998;29:89–95.
[19] Greengard LF, Rokhlin V. A fast algorithm for particle simulations. J Comput Phys 1987;73:325–48.
[20] Nakasone Y, Nishiyama H, Nojiri T. Numerical equivalent inclusion method: a new computational method for analyzing stress fields in and around inclusions of various shapes. Mater Sci Eng 2000;A285:229–38.
[21] Ma H, Yan C, Qin QH. Eigenstrain formulation of boundary integral equations for modeling particle-reinforced composites. Eng Anal Boundary Elem 2009;33:410–9.
[22] Qin QH. Nonlinear analysis of Reissner plates on an elastic foundation by the BEM. Int J Solids Struct 1993;30:3101–11.
[23] Ma H, Kamiya N. Boundary-type integral formulation of domain variables for three-dimensional initial strain problems. JSCE J Appl Mech 1998;1:355–64.
[24] Ma H, Zhou J, Qin QH. Boundary point method for linear elasticity using constant and quadratic moving elements. Adv Eng Softw 2010;41:480–8.
[25] Ma H, Kamiya N. A general algorithm for the numerical evaluation of nearly singular boundary integrals of various orders for two- and three-dimensional elasticity. Comput Mech 2002;29:277–88.